Realistic photoacoustic image simulations of collections of solid spheres using linear array transducer

Subhajit Karmakar[a], Eno Hysi[b], Michael C. Kolios[b,c] and Ratan K. Saha[d]

[a] University Science Instrumentation Centre, The University of Burdwan, Bardhaman, India;
[b] Department of Physics, Ryerson University, Toronto, Canada;
[c] Affiliate Scientist, Li Ka Shing Knowledge Institute/Keenan Research Center, St. Michaels Hospital, Toronto, Canada;
[d] Surface Physics and Material Science Division, Saha Institute of Nuclear Physics, Kolkata, India

ABSTRACT

A methodology for simulating photoacoustic (PA) images of samples with solid spherical absorbers acquired using linear array transducer is described. Two types of numerical phantoms (*i.e.* polystyrene beads suspended in agar medium) of two different size regimes were imaged with a 40 MHz linear array transducer utilizing this approach. The frequency domain features and statistics of the simulated signals were quantified for tissue characterization. The midband fit at 40 MHz was found to be about 35 dB higher for the sample with larger beads (radius $\sim 7.36\ \mu$m) than that of the sample with smaller particles (radius $\sim 1.77\ \mu$m). The scale parameter of the generalized gamma distribution function was found to be nearly 51 times greater for the former sample compared to the latter sample. The method developed here shows potential to be used as a fast simulation tool for the PA imaging of collection of absorbers mimicking biological tissue.

Keywords: Photoacoustics, B-mode image simulation, linear array transducer, spectral and statistical analysis

1. INTRODUCTION

Photoacoustic (PA) tomography has evolved to be an impactful class of biomedical imaging modalities over the last fifteen years.[1–4] Notable achievements have allowed various research groups to obtain volumetric images of organs, the vascular architecture of small animals and of the human arm.[1–3] Further, visualization of molecular biomarkers, induced thermal lesions, tumor vascularization have been accomplished using this technique.[4] Numerical simulations using the k-Wave tool box have also extensively been conducted to generate PA tomography images, optimize various parameters (such as laser arrangement and pulse length, receiver arrangement and bandwidth etc.) and to study the performance of reconstruction algorithms for PA tomography applications.[5]

Recently, an analytical model has been developed by exploiting a single particle approach to study PAs from an ensemble of discrete absorbers.[6] Essentially, the PA field for a collection of absorbers in this model is expressed as a summation of tiny fields emitted by the individual objects. The model has been widely applied in probing red blood cell (RBC) morphologies.[6,7] The potential of PA technique to detect malarial infection in blood has also been examined utilizing this model.[8] A theoretical framework for PA B-mode imaging with single element transducer has been proposed as well using this particle-based approach.[9] Moreover, this model in the framework of forward problem formulation revealed that ultrasonic spectral domain features of radio frequency (RF) PA signals depend on the properties of tissue microstructures and therefore, opened up a possibility that tissue characterization may be feasible with ultrasound resolution PAs. Recent experimental investigations provide encouraging results and thus, speculate great prospect of PA tissue characterization technique.[10–15] However, almost all the investigations into PA tissue characterization have utilized single element transducers given their simple geometry.

For further correspondence: ratank.saha@saha.ac.in, Telephone: 91 33 2337 5345

Photons Plus Ultrasound: Imaging and Sensing 2015, edited by Alexander A. Oraevsky, Lihong V. Wang
Proc. of SPIE Vol. 9323, 932339 · © 2015 SPIE · CCC code: 1605-7422/15/$18
doi: 10.1117/12.2080794

The purpose of this paper is two fold. First, we propose a theoretical framework for PA B-mode imaging of collection of discrete absorbers using a linear array transducer. It has been implemented here to simulate PA images of two different samples containing polystyrene beads of two different size regimes in agar medium (referred to as the Faran and the Rayleigh phantoms). Second, we extract spectral features and envelope statistics from the simulated RF lines for quantitative assessment of imaging media. Through such analysis we hope to expand on realistic PA investigations to characterize biological tissue using linear array transducer.

2. ANALYTICAL MODEL

2.1 PA pressure field from ensemble of single solid spheres

The analytical expression for the PA field emitted by a solid sphere, when it is suspended in a fluid medium and irradiated uniformly by a intensity modulated laser beam, can be found in the literature.[16] The linear superposition principle can further be used to derive the expression for the PA field generated by an ensemble of suspended solid spheres and it can be cast as,[6–8, 16]

$$\tilde{p}(\mathbf{r}_n,\omega) = BI_0 \sum_{s=1}^{N_s} \frac{j_1(\hat{q})}{A_1\frac{\sin\hat{q}}{\hat{q}} - A_2\cos\hat{q} + i\hat{\rho}\hat{v}[A_3\sin\hat{q} + A_4\cos\hat{q}]} \frac{e^{ik_f|\mathbf{r}_n-\mathbf{r}_s|}}{|\mathbf{r}_n-\mathbf{r}_s|}, \tag{1}$$

where, j_1 is the spherical Bessel function of first order and

$$B = \frac{iK\beta\mu a^2}{\rho_b C_P v_l}, \quad A_1 = (1-\hat{\rho}+\hat{\rho}\frac{\tilde{v}^2}{\hat{q}^2}), \quad A_2 = (1+\hat{\rho}\frac{\tilde{v}^2}{\hat{q}^2}), \quad A_3 = (1-\frac{\tilde{v}^2}{\hat{q}^2}), \quad A_4 = \frac{\tilde{v}^2}{\hat{q}},$$
$$\text{and} \quad \hat{q} = \omega a/v_l, \quad k_f = \omega/v_f, \quad \hat{\rho} = \rho_b/\rho_f, \quad \hat{v} = v_l/v_f, \quad \tilde{v} = 2v_t/v_l.$$

Here, a is the radius of the s-th sphere; K, β, C_P and μ are the bulk modulus, thermal expansion coefficient, heat capacity and light absorption coefficient for the solid medium, respectively; I_0 and ω are the intensity and modulation frequency of the laser beam; N_s is the total number of solid spheres present within ROI. Further, ρ_b, v_l and v_t denote the density, longitudinal and transverse sound speeds for the solid medium, respectively; ρ_f and v_f represent the density and speed of sound for the surrounding medium, respectively; $\mathbf{r}_s$ and $\mathbf{r}_n$ are the position vectors for the source and field points, respectively; $\mathbf{k}_f$ defines the direction of measurement. A schematic diagram is presented in Fig. 1. The time domain PA response for a delta function deposition of heat can be obtained using the Fourier transformation of Eq. (1) as,

$$p(\mathbf{r}_n,t) \;=\; \frac{BF}{2\pi}\sum_{s=1}^{N_s}\int_{-\infty}^{\infty} d\omega\; p_s(\omega)e^{-i\omega t}\; \frac{e^{ik_f|\mathbf{r}_n-\mathbf{r}_s|}}{|\mathbf{r}_n-\mathbf{r}_s|}, \tag{2}$$

where F is the optical fluence and $p_s(\omega) = \frac{j_1(\hat{q})}{A_1\frac{\sin\hat{q}}{\hat{q}} - A_2\cos\hat{q} + i\hat{\rho}\hat{v}[A_3\sin\hat{q}+A_4\cos\hat{q}]}$.

2.2 PA signal detection by linear array transducer

Since we are simulating the PA signal detected by a linear array transducer, the measured signal $p_n(t)$ by the n-th array element is proportional to the spatially averaged PA pressure over the aperture area A of the transducer element and it can be written as,

$$\begin{aligned} p_n(t) &= \frac{2\pi}{A}\frac{BF}{2\pi}\sum_{s=1}^{N_s}\int\int d^2\mathbf{r}_n \int_{-\infty}^{\infty} d\omega\; p_s(\omega)e^{-i\omega t}\; \frac{e^{ik_f|\mathbf{r}_n-\mathbf{r}_s|}}{2\pi|\mathbf{r}_n-\mathbf{r}_s|}, \\ &= \frac{2\pi}{A}\frac{BF}{2\pi}\sum_{s=1}^{N_s}\int_{-\infty}^{\infty} d\omega\; p_s(\omega)e^{-i\omega t}\; H_D(\omega), \end{aligned} \tag{3}$$

where $H_D(\omega) = \int\int \frac{e^{ik_f|\mathbf{r}_n-\mathbf{r}_s|}}{2\pi|\mathbf{r}_n-\mathbf{r}_s|}\, d^2\mathbf{r}_n$ is the directivity function of the n-th array element.[17] Using the property of the Fourier transformation, an equivalent expression for Eq. (3) can be deduced as,

$$p_n(t) = \frac{2\pi}{A}\sum_{s=1}^{N_s}\left[p_s(t) *_t h(\mathbf{r}_s,\; t)\right], \tag{4}$$

where

$$p_s(t) = \frac{BF}{2\pi} \int_{-\infty}^{\infty} d\omega \; p_s(\omega) e^{-i\omega t}, \quad \text{and} \quad h(\mathbf{r}_s, t) = \int\int \frac{\delta\left(t - |\mathbf{r}_n - \mathbf{r}_s|/v_f\right)}{2\pi |\mathbf{r}_n - \mathbf{r}_s|} d^2\mathbf{r}_n, \tag{5}$$

is the spatial impulse response function (SIRF) of the n-th receiver[17] and $*_t$ denotes temporal convolution. The corresponding geometry is displayed in Fig. 1. Even though Eq. 4 represents a complex signal, PA pressure signals are real and detected by an ultrasound transducer with finite receiving bandwidth. The frequency response of a transducer can be modeled using the Gaussian functions for which time domain impulse response be expressed as,[8,9]

$$g_R(\omega_0, \xi, t) = \frac{\xi}{\sqrt{2\pi}} e^{-\frac{\xi^2 t^2}{2}} \cos(\omega_0 t), \qquad g_I(\omega_0, \xi, t) = \frac{\xi}{\sqrt{2\pi}} e^{-\frac{\xi^2 t^2}{2}} \sin(\omega_0 t), \tag{6}$$

where ω_0 is the center frequency and ξ is the -6 dB bandwidth. A bandlimited (BL) radio frequency (RF) signal $p_n^{BL}(t)$ detected by the n-th element can be calculated by convolving the real part of $p_n(t)$ with g_R as,[8,9]

$$p_n^{BL}(t) = Re\{p_n(t)\} *_t \; g_R(\omega_0, \xi, t). \tag{7}$$

2.2.1 Delay and sum beamforming

A linear array consists of periodically arranged N number of small active elements. A sub-aperture of N_A elements is used to dynamically focus a space point and construct a beamformed (BF) RF line for imaging. It is evident from the array geometry (Fig. 1) that the PA signal $p_n^{BL}(t)$ originating from a source location at $\mathbf{r}_m$ arrives the n-th element at time $t_m = \frac{|\mathbf{r}_n - \mathbf{r}_m|}{v_f}$. But, the signal will be delayed by an amount of $\tau_n = \frac{|\mathbf{r}_{n+1} - \mathbf{r}_m| - |\mathbf{r}_n - \mathbf{r}_m|}{v_f}$ to reach the (n+1)-th element of the array due to the path difference between source to observation points for two different elements. Therefore, to focus a space point $\mathbf{r}_m$, relative delays between the group of active array elements need to be compensated before adding their responses with different weights W_n (beam-shape depends on the weight factors[18]). The resultant PA pressure under delay and sum beamforming can be written as,[18]

$$p^{BF}(t_m) = \sum_{n=0}^{N_A - 1} W_n \; p_n^{BL}(t_m - \tau_n), \tag{8}$$

and consequently the beamformed RF line for many such space points can be found as,

$$p^{BF}(t) = \sum_{n=0}^{N_A - 1} W_n \; p_n^{BL}(t - \tau_n). \tag{9}$$

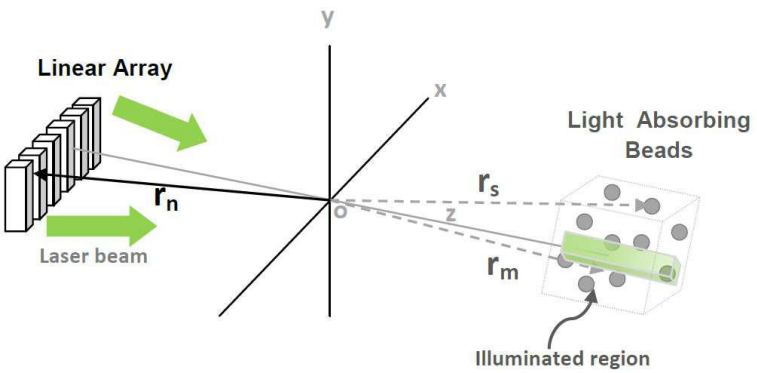

Figure 1. Schematic of PA imaging geometry.

The envelope of BF line can be obtained using the BL Hilbert transform pairs of Eq. (9) as,

$$E(t) = \sqrt{\left(p^{BF}(t) *_t g_R\right)^2 + \left(p^{BF}(t) *_t g_I\right)^2}. \tag{10}$$

Eq. (10) constitutes the mathematical framework for calculating envelopes of BF BL PA RF lines for a collection of uniformly illuminated solid spheres when detected by linear array transducer.

3. MATERIALS AND METHODS

3.1 Phantom and simulation parameters

Two numerical phantoms were generated using black polystyrene beads of different sizes following a recent experimental work.[13] Each bead was considered as a solid sphere of radius either 7.36 μm or 1.77 μm in order to inspect different size regimes (*viz.* the Faran and the Rayleigh particles). The corresponding size parameters at 40 MHz could be calculated to be $k_f a = 1.20$ and 0.29, respectively. A Monte Carlo method[19] known as the random adsorption technique was used to generate random positions of beads to fill a volume of $15 \times 0.5 \times 5$ mm^3. A total number of 656,200 beads were placed within ROI for each phantom. Accordingly, volume fractions occupied by beads became approximately 0.04 and 2.9%, respectively. The numerical values of density, longitudinal and transverse sound speeds for bead were taken from the literature[13] as $\rho_b = 1050$ kg/m^3, $v_l = 2350$ m/s, $v_t = 1120$ m/s, respectively; the density and the speed of sound for the surrounding fluid medium were taken as $\rho_f = 1005$ kg/m^3 and $v_f = 1540$ m/s, respectively. The numerical values of these parameters were fixed based on the above mentioned experimental work. The parameters K, β, C_P, μ and F only control the amplitude of the emitted PA signal and do not change the frequency content of the signal. Therefore, these parameters were treated as constants in this study.

3.2 Linear array specifications

A linear array transducer consisting of 256 elements and center frequency of 40 MHz was used to detect PA signals. The -6 dB bandwidth was 24 MHz. The size of each array element was taken as 38.5 x 385 μm^2 and the spacing between two adjacent elements was fixed at 19.25 μm. A BF line was constructed for a sub-aperture of 64 elements. These specifications correspond to one of the arrays of a commercial PA imaging system.[20]

3.3 Imaging algorithm

The ROI was divided into a number of equal sized boxes of size approximately $0.078 \times 0.05 \times 5$ mm^3 along the x-direction (see Fig. 1). A laser beam uniformly illuminated this volume. The irradiated region is highlighted in Fig. 1. PA waves, emitted by 3400 number of beads randomly located inside the irradiated volume and propagated along the -z-direction, were received by the sub-aperture of the linear array transducer. A well-known software Field II was employed to calculate SIRF for each element.[17] The contributions from a wide range of frequencies (0.001 to 2000 MHz with a step of 0.5 MHz) were summed up while calculating Eq. (4). A sampling frequency of 4 GHz was used. BL transducer response was obtained according to Eq. (8). The Gaussian window of the filtering functions was truncated up to $\pm$ 4ξ length (ξ was taken as the 60% of the center frequency). Each BL RF line was further decimated by a factor of 20 while performing delay and sum operations over the individual PA signals received by the elements in the sub-aperture. Initially, 193 such scan lines along the x-direction were computed for the entire phantom volume (*i.e.* $15 \times 0.05 \times 5$ mm^3). However, 100 lines about the center of the array were taken for imaging which corresponded to a volume of $7.8 \times 0.05 \times 5$ mm^3. The envelope of each BF scan line was determined using the Hilbert transform pairs as given in Eq. (10). Log compression and interpolation along the x-direction were performed to obtain a 40 dB dynamic range B-Mode PA images of the numerical phantoms and 256 gray levels were used to encode dynamic range.

3.4 Envelope statistics and spectral parameters

The average envelope histogram was computed from 100 simulated BF lines and it was fitted with the generalized gamma (GG) distribution function given by,

$$f(A) = \frac{cA^{cu-1}}{\alpha^{cu}\Gamma(u)} \exp(-\frac{A^c}{\alpha^c}), \quad A \geq 0, \quad \alpha, c, u > 0, \tag{11}$$

where α is the scale parameter; c and u are the shape parameters. The best fit parameters were obtained by using a MATLAB routine (*i.e. fminsearch*).

The region considered for imaging (*i.e.* $7.8 \times 0.05 \times 5$ mm^3) was divided into 10 boxes of equal size (5 boxes along the x-direction and 2-boxes along the z-direction). Each box enclosed 20 RF lines. An average power spectrum was obtained from those lines and that was normalized by a reference spectrum. The reference spectrum was generated from a polystyrene bead of 10 μm radius, embedded in agar medium and illuminated with the same laser beam. The normalized spectrum within -6 dB bandwidth of the transducer (28 to 52 MHz) for each box was fitted with a straight line. The quantitative values of midband fit and spectral slope were evaluated. These values were compared for 10 different regions.

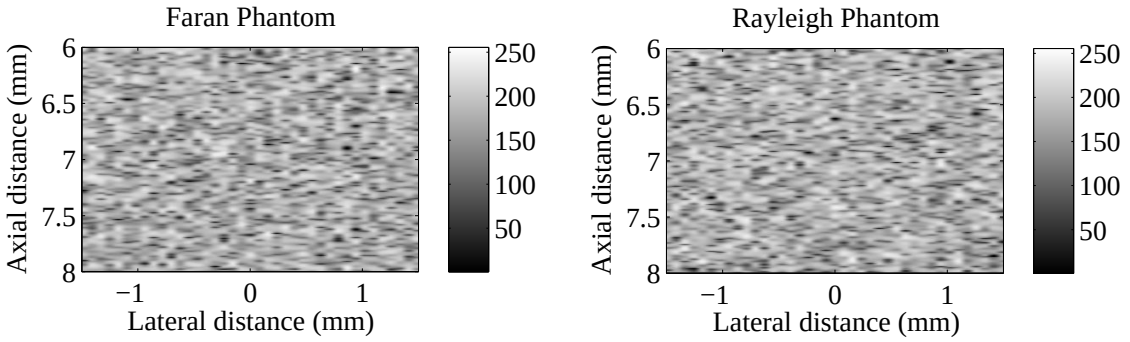

Figure 2. Simulated PA images of the ensemble of the Faran and the Rayleigh type absorbers. The dynamic range is about -40 dB. Small region is shown in each figure to improve its clarity. However, tissue characterization analysis was performed using raw RF lines.

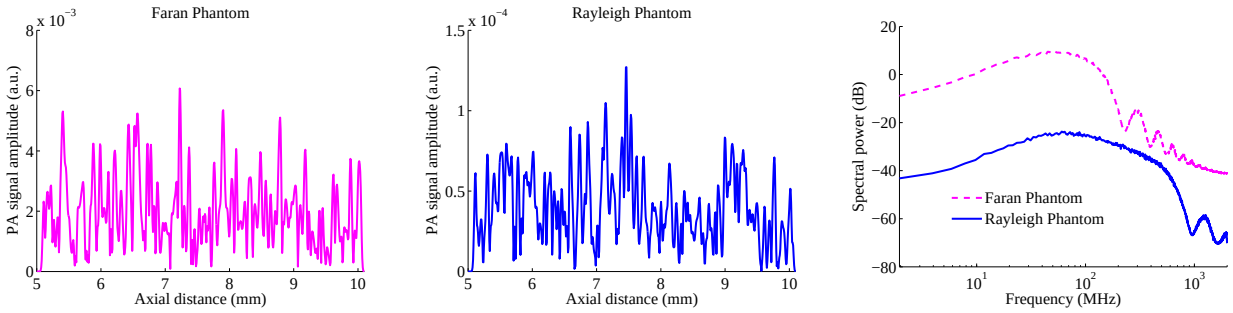

Figure 3. Representative plots of simulated envelopes for the Faran (left panel) and the Rayleigh (middle panel) phantoms. A single trace is shown in each figure. Plots of average spectra (computed from simulated BF RF lines sampled at 4 GHz) for those phantoms (right panel).

4. RESULTS AND DISCUSSION

Fig. 2 displays simulated images of the phantoms. The dynamic range is -40 dB in each figure. A small portion of the entire phantom is shown in each figure in order to improve visibility. It is clear that fully developed

speckles are present in the figures. This is consistent with experimental observation.[13] Although the Faran type beads are nearly 4.16 times larger in size than that of the Rayleigh type, negligible difference is observed between the gray scale PA images. However, the difference lies in the generated RF lines plotted in Fig. 3. These are BL and decimated signals as described above. The average amplitude of the PA signal for the Faran phantom is significantly higher than that of the Rayleigh phantom because particle size is larger in the former case. The average power spectrum for each phantom is also outlined in Fig. 3. As expected, spectral power at each frequency up to 100 MHz is greater for the Faran phantom than the Rayleigh phantom.

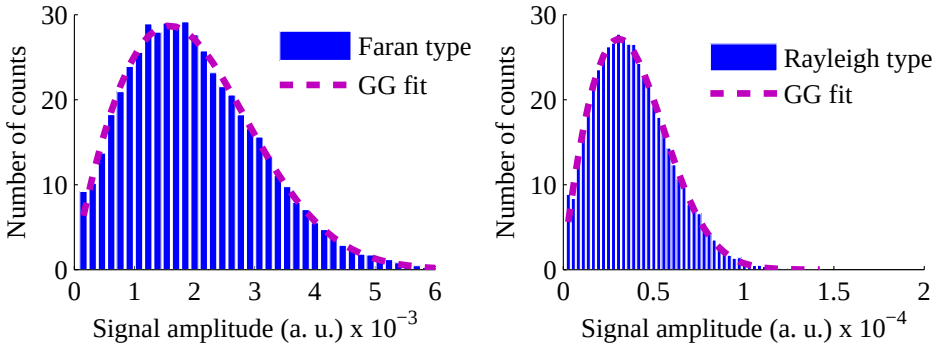

Figure 4. GG fit to the envelope histograms for the Faran phantom and the Rayleigh phantom.

Table 1. Parameters of GG distribution fit.

	Faran Phantom	Rayleigh Phantom
Scale parameter (α)	$2.48\text{x}10^{-3}$	$4.88\text{x}10^{-5}$
Shape parameter (c)	2.12	2.22
Shape parameter (u)	0.86	0.82

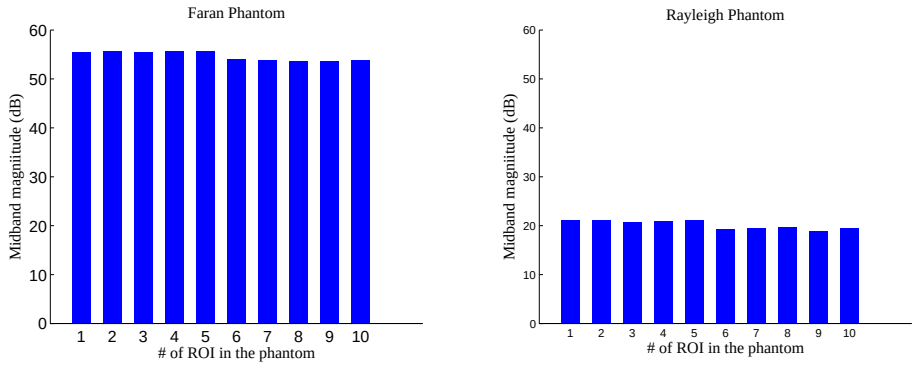

Figure 5. Midband (28-52 MHz) fit magnitude of the simulated spectrum of the Faran phantom (left panel) and the Rayleigh phantom (right panel).

Fig. 4 shows GG distribution fits to the histograms computed from the envelope of 100 RF lines corresponding to the Faran and the Rayleigh phantoms. The best fit parameters are presented in Table 1. The scale parameter is approximately 51 times higher for the Faran spheres compared to the Rayleigh beads. However, the shape parameters are comparable. The ratio of c to u can be calculated to be 2.46 and 2.70 for those samples,

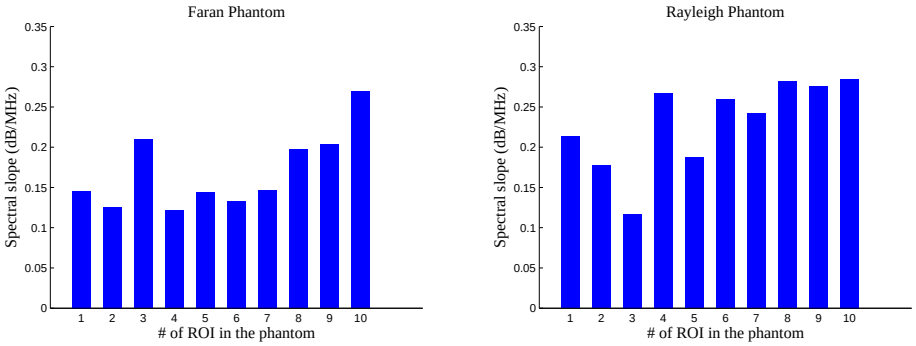

Figure 6. Spectral slope of the midband (28-52 MHz) fit line of the simulated spectrum of the Faran phantom (left panel) and the Rayleigh phantom (right panel).

respectively. This ratio c/u is known to depend on the number density of the particles.[13] They are similar because particle number density is the same for the both types of numerical phantoms. Each of them contained 656,200 beads inside the entire volume as mentioned above.

Fig. 5 plots the midband fit for 10 sub-regions of the entire imaging volume for each phantom. Corresponding values of spectral slope is illustrated in Fig. 6. The midband fit does not vary significantly over the sub-regions in each case. The average difference is about 35 dB between the phantoms. The spectral slope exhibits small variation (0.12 to 0.27 dB/MHz) over the sub-regions for the Faran sample owing to the fact that spatial arrangement of beads may differ slightly in different sections. Similar trend can also be seen for the Rayleigh case. Additionally, average spectral slope for the latter case is slightly higher in comparison to the former case. This is likely due to size difference of absorbers (*e.g.* $a = 1.77$ and 7.36 μm for the Rayleigh and the Faran particles, respectively).

5. CONCLUSIONS

A theoretical framework is presented in detail for PA B-mode imaging of collection of solid beads using linear array transducer. The tiny signals generated by individual beads are added linearly to obtain a resultant RF line. The delay and sum beamforming algorithm has been incorporated to dynamically focus various space points. The approach has been implemented here to simulate PA images of collection of polystyrene beads embedded in agar medium by a clinically relevant linear array transducer of center frequency 40 MHz. It is a very fast method (computation of a line needed approximately 1 minute in a personal computer). The results of the envelope statistics demonstrate that the scale parameter of GG distribution is 51 times greater for the Faran phantom (bead radius ~ 7.36 μm) than the Rayleigh phantom (bead radius ~ 1.77 μm). The midband fit parameter at 40 MHz is computed to be 35 dB higher for the Faran phantom than the Rayleigh phantom confirming that tissue characterization method may be applied to classify imaging media in practice. This methodology has the potential to simulate PA images of samples of irregular, non-uniform geometries containing regular light absorbing objects in a realistic time frame.

ACKNOWLEDGMENTS

This research was undertaken, in part, thanks to funding from NSERC (grant #216986-2012) and the Canada Research Chairs Program awarded to M Kolios. Funding to purchase the equipment was provided by the Canada Foundation for Innovation, the Ontario Ministry of Research and Innovation, and Ryerson University. R K Saha would like to thank CSIR, New Delhi for funding.

REFERENCES

[1] H. F. Zhang, K. Maslov, G. Stoica and L. V. Wang, "Functional photoacoustic microscopy for high-resolution and noninvasive *in vivo* imaging", Nat. Biotechnol., 24(7), 848-851 (2006).

[2] L. V. Wang and S. Hu, "Photoacoustic Tomography: In Vivo Imaging of Organelles to Organs", Science, 335, 1458-1462 (2012).

[3] P. Beard, "Biomedical photoacoustic imaging", Interface Focus, 1, 602-631 (2011).

[4] J. Gateau, M. Á. A. Caballero, A. Dima and V. Ntziachristos, "Three-dimensional optoacoustic tomography using a conventional ultrasound linear detector array: Whole-body tomographic system for small animals", Med. Phys., 40(1), 013302 (2013).

[5] B. Cox and P. C. Beard, "Modeling of photoacoustic propagation in tissue using k-space techniques", in L. V. Wang edited, "Photoacoustic imaging and spectroscopy", Taylor & Francis Group, LLC, pp. 25-34 (2009).

[6] R. K. Saha and M. C. Kolios, "A simulation study on photoacoustic signals from red blood cells", J. Acoust. Soc. Am, 129(5), 2935-2943 (2011).

[7] E. Hysi, R. K. Saha and M. C. Kolios, "On the use of photoacoustics to detect red blood cell aggregation", Biomed. Opt. Exp., 3(9), 2326-2338 (2012).

[8] R. K. Saha, S. Karmakar and M. Roy, "Computational investigation on the photoacoustics of malaria infected red blood cells", PLoS ONE, 7(12), e51774 (2012).

[9] S. Karmakar, M. Roy and R. K. Saha, "Photoacoustic imaging of nanoparticle containing cells using single element focused transducer: A simulation study", IEEE Trans. Ultrason. Ferroelectr. Freq. Control, in press.

[10] R. E. Kumon, C. X. Deng and X. Wang, "Frequency-domain analysis of photoacoustic imaging data from prostate adenocarcinoma tumors in a murine model", Ultrasound in Med. and Biol., 37(5), 834-839 (2011).

[11] S. Wang, C. Tao, X. Wang and X. Liu, "Quantitative detection of stochastic microstructure in turbid media by photoacoustic spectral matching", Appl. Phys. Lett., 102, 114102 (2013).

[12] P. V. Chitnis, J. Mamou, A. Sampathkumar and E. J. Feleppa, "Spectrum analysis of photoacoustic signals for tissue classification", Proc. of SPIE, 8943, 89432J-1-7 (2014).

[13] E. Hysi, D. Dopsa and M. C. Kolios, "Photoacoustic tissue characterization using envelope statistics and ultrasonic spectral parameters", Proc. of SPIE, 8943, 89432E-1-9 (2014).

[14] M. P. Patterson, C. B. Riley, M. C. Kolios and W. M. Whelan, "Optoacoustic characterization of prostate cancer in an in vivo transgenic murine model", J Biomed Opt., 19(5), 056008 (2014).

[15] M. Alhamami, M. C. Kolios and J. Tavakkoli, "Photoacoustic detection and optical spectroscopy of high-intensity focused ultrasound-induced thermal lesions in biologic tissue", Med. Phys., 41(5), 053502 (2014).

[16] M. I. Khan and G. J. Diebold, "The photoacoustic effect generated by an isotropic solid sphere", Ultrasonics, 33(4), 265-269 (1995).

[17] J. A. Jensen, "Linear description of ultrasound imaging systems", Notes for the International Summer School on Advanced Ultrasound Imaging, Technical University of Denmark July 5 to July 9, 1999, Technical University of Denmark (June, 2001).

[18] T. L. Szabo, Chapter 7 in Diagnostic ultrasound imaging: Inside out, Elsevier Academic Press, New York, pp. 171 to 212 (2004).

[19] E. L. Hinrichsen, J. Feder and T. Jøssang, "Random packing of disks in two dimensions", Phys. Rev. A, 41(8), 4199-4209 (1990).

[20] A. Needles, A. Heinmiller, J. Sun, C. Theodoropoulos, D. Bates, D. Hirson, M. Yin and F. Stuart Foster, "Development and initial application of a fully integrated photoacoustic micro-ultrasound system", IEEE Trans. Ultrason. Ferroelectr. Freq. Control, 60(5), 888-889 (2013).